IOP Publishing Smart Materials and Structures
Smart Mater. Struct. **26** (2017) 037002 (9pp) https://doi.org/10.1088/1361-665X/aa5a35

Technical Note

Geometric scaling of artificial hair sensors for flow measurement under different conditions

Weihua Su[1] **and Gregory W Reich**[2]

[1] University of Alabama, Department of Aerospace Engineering and Mechanics, Tuscaloosa, AL 35487, United States of America
[2] US Air Force Research Laboratory, Aerospace Systems Directorate, Wright-Patterson AFB, OH 45433, United States of America

E-mail: suw@eng.ua.edu

Received 19 October 2016, revised 16 December 2016
Accepted for publication 18 January 2017
Published 13 February 2017

Abstract

Artificial hair sensors (AHSs) have been developed for prediction of the local flow speed and aerodynamic force around an airfoil and subsequent application in vibration control of the airfoil. Usually, a specific sensor design is only sensitive to the flow speeds within its operating flow measurement region. This paper aims at expanding this flow measurement concept of using AHSs to different flow speed conditions by properly sizing the parameters of the sensors, including the dimensions of the artificial hair, capillary, and carbon nanotubes (CNTs) that make up the sensor design, based on a baseline sensor design and its working flow condition. In doing so, the glass fiber hair is modeled as a cantilever beam with an elastic foundation, subject to the distributed aerodynamic drag over the length of the hair. Hair length and diameter, capillary depth, and CNT height are scaled by keeping the maximum compressive strain of the CNTs constant for different sensors under different speed conditions. Numerical studies will demonstrate the feasibility of the geometric scaling methodology by designing AHSs for aircraft with different dimensions and flight conditions, starting from the same baseline sensor. Finally, the operating bandwidth of the scaled sensors are explored.

Keywords: geometric scaling, artificial hair sensor, flow measurement, boundary layer

(Some figures may appear in colour only in the online journal)

1. Introduction

'Fly-by-feel' technologies have been developed for agile aircraft systems. With such technology, aerodynamic forces on aircraft lifting surfaces may be directly measured and used for the robust flight control. It is hoped that the fly-by-feel technology may enhance the aircraft safety and maneuverability. For a better control of the aircraft behavior, more accurate information about the flow condition is always desired. For this purpose, different flow measurement approaches, including pressure sensors [1–3], have been explored to obtain real-time, *in situ* air flow information on or near wing surfaces. In reality, natural flight systems use redundant control and estimation mechanisms [4]. For example, bats utilize hairs to sense the air turbulence [5] and feed back to their own control system. The most important advantage of redundant sensing systems is their robustness. In addition, redundant sensing systems may provide more information about sensor data's temporal and spatial distribution, which is difficult to obtain from point sensors. Inspired by the fact that natural flyers use hairs to sense and feedback flow conditions to help maintain the flight quality, people have developed artificial hair sensors (AHSs) to collect flow information data around structures [6–10]. Specifically, a research group at the US Air Force Research Laboratory have

designed and constructed AHSs from micro-scale, S-2 glass fibers coated with a radially aligned carbon nanotube (CNT) forest. Electrodes in an accompanying capillary allow for a piezoresistive response from the compression of the CNTs when the hair is deflected by the air flow [11]. Correlations between the flow visualization using particle image velocimetry and the sensor measurement have indicated the feasibility of AHS measurements in collecting the flow information [11].

However, a specific design of the hair sensor is usually sensitive only to its specific working region of the flow condition and speed. It is obvious that the geometry and properties of the hair, capillary, and CNT may significantly impact the operating/sensitive region of AHSs. Even though the AHS concept is promising to provide a robust control mechanism for different sizes of aircraft, people still have to make suitable designs of AHSs based on the specific geometry and flight condition of the vehicles where the AHSs are going to be applied to.

Following the geometrical scaling approach for AHSs developed in a previous study [12], the hair made of glass fiber is modeled as a linear Euler–Bernoulli beam with an elastic foundation due to the CNT forest, subject to aerodynamic drag over the length of the hair. The drag is obtained by assuming a laminar boundary layer with a very low Reynolds number. The hair is deflected due to the drag and compresses the CNTs inside the capillary. The maximum compressive strain of CNTs is then used to scale the geometrical parameters of hairs that work at different flow conditions. The numerical study will demonstrate the feasibility of the scaling design approach with additional exploration on the operating bandwidths of the scaled sensors.

2. Theoretical formulation

The linear Euler–Bernoulli beam theory with an elastic foundation is applied in the modeling of AHSs, subject to the aerodynamic drag due to the air flow determined from the laminar boundary layer. The criterion for the scaling design of the hair sensors is then introduced based on the structural model.

2.1. Structural modeling of AHSs

A hair sensor model is shown in figure 1. An artificial hair made of glass fiber is inserted in a capillary hole, where the lengths of the hair inside the capillary and exposed in the air are l_1 and l_2, respectively. The diameter of the hair is d and the inner diameter of the capillary is D. CNTs are radially grown along the hair and are assumed to be perfectly limited within the capillary. The hair compresses the CNTs as it is deflected by the local flow of pressure $p(x)$. As a reaction, CNTs act as springs (with the constant k) to resist the hair deformation. As introduced in Phillips *et al* [11], the compression of CNTs causes the piezoelectric resistive effects of the electrode mounted inside the capillary, which can be measured from the electric current passed through the sensor and calibrated to the local flow speed.

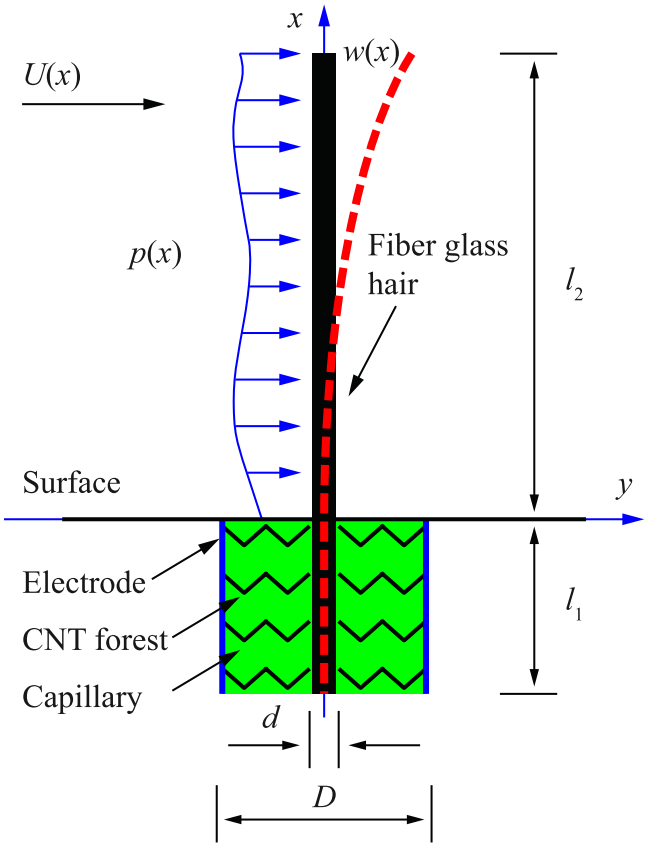

Figure 1. Description of an AHS model.

For design and estimation of the sensor performance, the artificial hair is modeled as a uniform beam with a partial Winkler foundation of stiffness k, as suggested by Slinker *et al* [13] and Phillips *et al* [14]. For simplicity, the beam is considered linear and the Euler–Bernoulli Beam formulation is used:

$$EI\frac{\mathrm{d}^4 w(x)}{\mathrm{d}x^4} + kw(x) = p(x), \tag{1}$$

where w is the deflection of the hair and EI is the bending rigidity of the hair, determined by the Young's modulus and diameter of glass fiber hair. The spring constant k measured per unit span is obtained by the properties of CNTs [13, 14], given as

$$k(D, d) = \frac{\pi\kappa r}{2(R - r)} = \frac{\pi}{2}\frac{d}{D - d}\kappa, \tag{2}$$

where $\kappa = \kappa(D, d)$ is the compressive modulus of CNTs. It is dependent on the height of the CNT forest [15] and thus a function of the diameters D and d. Therefore, the equivalent spring constant of the elastic function is not constant during the scaling process.

The beam deflection is solved individually on $x \in [-l_1, 0]$ and $x \in [0, l_2]$. On $x \in [-l_1, 0]$, the analytical solution of the beam deflection is

$$w(x) = \mathrm{e}^{\beta x}[C_1 \sin(\beta x) + C_2 \cos(\beta x)] + \mathrm{e}^{-\beta x}[C_3 \sin(\beta x) + C_4 \cos(\beta x)], \tag{3}$$

where

$$\beta = \sqrt[4]{\frac{k}{4EI}}. \tag{4}$$

The constants C_1 to C_4 are determined by the boundary conditions of the beam segment. The boundary condition at the bottom of the capillary ($x = -l_1$) depends on the contact between the hair and bottom surface, which may be an intermediate state between a fully clamped end and a free end. However, it is simplified as a cantilever in this work. The force boundary condition at $x = 0$ is obtained from the resultant load of the hair segment exposed in the air, which are

$$\begin{aligned} EI\frac{\mathrm{d}^3 w}{\mathrm{d}x^3}\bigg|_{x=0} &= F_0 = \int_0^{l_2} p(x)\mathrm{d}x \\ &= \int_0^{l_2} \frac{1}{2}\rho U^2(x) dc_d(x)\mathrm{d}x, \\ -EI\frac{\mathrm{d}^2 w}{\mathrm{d}x^2}\bigg|_{x=0} &= M_0 = \int_0^{l_2} p(x)x\mathrm{d}x \\ &= \int_0^{l_2} \frac{1}{2}\rho U^2(x) dc_d(x)x\mathrm{d}x, \end{aligned} \tag{5}$$

where $U(x)$ is the local flow speed at different heights of the hair segment exposed in the air and c_d is the drag coefficient around the cylindrical hair. If the flow is uniform, the boundary loads are

$$F_0 = pl_2,\ M_0 = \frac{1}{2}pl_2^2,\ p = \frac{1}{2}\rho U^2 dc_d. \tag{6}$$

The solution on $x \in [0, l_2]$ is given as

$$w(x) = w_0 + w_0' x + \frac{pl_2^2}{4EI}x^2 - \frac{pl_2}{6EI}x^3 + \frac{p}{24EI}x^4 \tag{7}$$

if uniform flow is assumed. Quantities w_0 and w_0' are the deflection and slope at $x = 0$, respectively, which are both solved from the equilibrium of the hair segment within the capillary ($x \in [-l_1, 0]$).

2.2. Local flow condition and its impact on AHS loads

In reality, due to the viscous effect of the flow in the boundary layer, the flow around the hair is never uniform (figure 2). A cubic speed profile in a laminar boundary layer over a flat plate is applied in this study:

$$U(x) = U_\infty\left[\frac{3}{2}\left(\frac{x}{\delta_l}\right) - \frac{1}{2}\left(\frac{x}{\delta_l}\right)^3\right], \tag{8}$$

where U_∞ is the magnitude of the free stream velocity and δ_l is the laminar boundary layer thickness at which $U(x)$ reaches $0.99U_\infty$, which is

$$\delta_l = 4.91\sqrt{\frac{\nu y_{\mathrm{le}}}{U_\infty}} = \frac{4.91 y_{\mathrm{le}}}{\sqrt{Re_y}}, \tag{9}$$

where y_{le} is the location of the hair downstream from the start of the boundary layer (assumed to be the leading edge of an airfoil) and ν is the kinematic viscosity of the air. Outside of the boundary layer, the airflow speed is simply the same as the free stream speed. It is also important to note that the flow within the boundary layer may transition from laminar to turbulent at

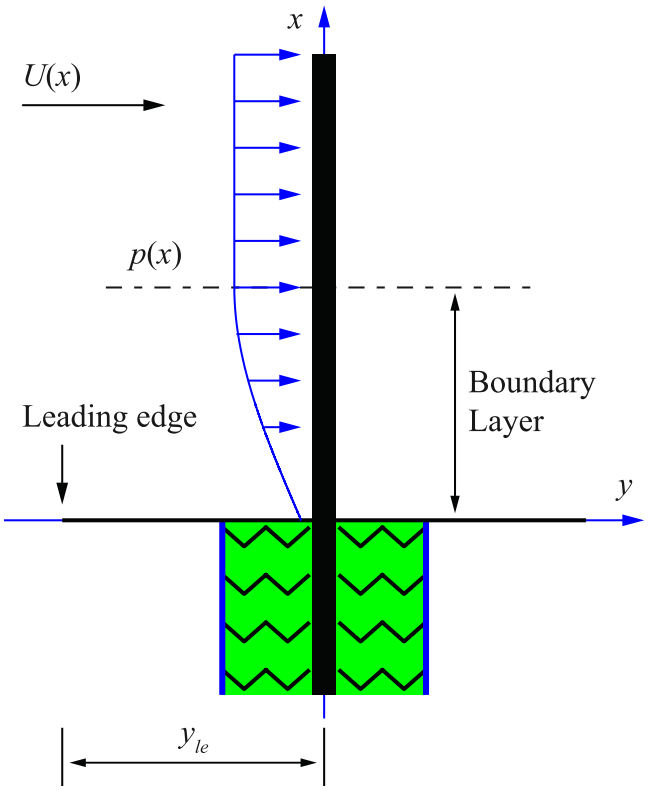

Figure 2. AHS in a shear flow across the boundary layer.

$$y_{\mathrm{tr}} = \frac{Re_{\mathrm{tr}}\nu}{U_\infty} \tag{10}$$

from the leading edge, where the Reynolds number for the transition is $Re_{\mathrm{tr}} = 5 \times 10^5$. Then the thickness of the turbulent boundary layer is estimated as

$$\delta_t = \frac{0.382 y_{\mathrm{le}}}{\left(\frac{U_\infty y_{\mathrm{le}}}{\nu}\right)^{0.2}}. \tag{11}$$

The above aerodynamic equations are based on the flow over a flat plate. For an airfoil, the local flow speed to be measured by the sensor is no longer equal to the free steam speed. The boundary layer thickness variation may also be different from that of a flat plate. For simplicity, equations (9)–(11) will be applied using the nominal free stream speed U_∞ to determine the boundary layer thickness. However, the shear flow speed distribution in the boundary layer will be determined by the local speed to be measured by the sensor, i.e.,

$$U(x) = U_m\left[\frac{3}{2}\left(\frac{x}{\delta_l}\right) - \frac{1}{2}\left(\frac{x}{\delta_l}\right)^3\right]. \tag{12}$$

Lastly, the drag coefficient c_d around the hair is dependent on the flow condition at different spanwise positions of the hair. According to Maschmann *et al* [15], it is determined by the

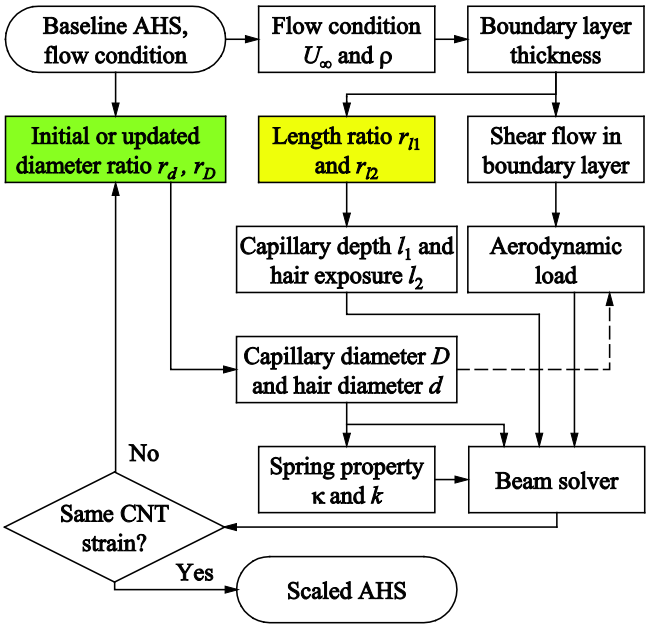

Figure 3. Flowchart of the scaling process for AHSs.

Reynolds number at the spanwise positions along the hair

$$c_d(x) = \exp\left(-\frac{2}{3}\ln Re_x(x) + \frac{5}{2}\right),$$
$$Re_x(x) = \frac{U(x)d}{\nu}. \tag{13}$$

A close-form solution of the deflection on $x \in [0, l_2]$ is generally not available, as the pressure distribution along the hair is not uniform. Instead, the solution can be obtained numerically. Nonetheless, the integrals in equation (5) can still be completed analytically, since the flow speed distribution in the boundary layer can be obtained analytically from equation (12). Therefore, a close-form solution of the deformation of the hair segment inside the capillary is always available as shown in equation (3).

2.3. Scaling design of AHSs under different flow conditions

Once an AHS is exposed in the air flow, the aerodynamic force acting on the sensor will bend the hair and compress the CNTs. The electrode mounted at the wall of the capillary will sense the compression and convert the signal to the change of the electric current. For a specific hair sensor length, there is a flow speed range where the hair is sensitive to the flow speed change. If the local flow speed is too low, the hair is not being deflected by the flow. Thus, the sensors are not able to measure the flow speed at all. On the other hand, if the flow speed becomes too high, the hairs may touch the wall of capillary or are even flattened onto the wing surface. In either situation, the sensors are saturated and cannot measure the flow speed. The design of AHSs in this work is focused on keeping the scaled AHSs within the active sensing range for a given local flow velocity. As the measurement data of AHSs are related to the compressive strain of the CNTs, the scaling design of AHSs will keep the CNT strain constant. The maximum compressive strain of CNTs is

$$\varepsilon = \frac{2w(0)}{D-d}, \tag{14}$$

where $w(0)$ is the hair deflection at $x = 0$.

When an AHS is scaled, the flow condition and thus the expected local speed and air density are firstly determined by the known flow condition of the different aircraft. These are used to estimate the boundary layer thickness and the shear flow distribution. The boundary layer thickness is then used to determine the length ratios of the hair (r_{l1} and r_{l2}). The design routine is finally set up to find the corresponding ratios of diameters r_d and r_D, so as to keep the same maximum CNT strain under the new flow condition. Note that the compressive modulus κ of CNTs increases with the CNT height of $(D-d)/2$, which in turn impacts the equivalent spring constant k. Figure 3 illustrates the scaling procedure of AHSs starting from a combination of known parameters of a baseline AHS.

3. Numerical studies

In this section, the structural model for AHSs is applied to the scaling design for the flow measurement of three different classes of aircraft. Some practical considerations are also discussed in this section.

3.1. Baseline AHS model

A baseline AHS model has been developed for flow measurement of a wing segment with a chord length of 0.1 m. The nominal flow condition is $U_\infty = 2.0\,\mathrm{m\,s^{-1}}$ at sea level, with an operating flow speed range from 1.4 to $2.6\,\mathrm{m\,s^{-1}}$, as the baseline AHS is sensitive to the flow speed changes in this range. With the nominal flow speed U_∞, the boundary layer thickness (figure 4) is estimated by using the laminar flow equation as the Reynolds number along the chord is always less than the critical number of transition. Ideally, the length of a hair installed at a specific chordwise position should relate to the corresponding boundary layer thickness and the hair should stick out of the boundary layer. For simplicity, only one hair installed at a quarter chord from the leading edge is studied here. In addition, the hair length exposed in the air (l_2) is required to be $1/3$ longer than the local boundary layer thickness (figure 4). While this is an arbitrary requirement, it represents a reasonable assumption in order to complete the scaling analysis. In fact, the hair length should be at least greater than the boundary layer thickness, in order to for the sensor to measure the free stream. However, if the hair is too long, it is easy to be flattened onto the wing surface, reducing the measuring bandwidth (sensitivity range) of the sensor. The aforementioned arbitrary requirement will be shown to be a reasonable choice in the following studies, resulting good measurement bandwidth of the scaled sensors. Other geometric and material parameters of the baseline AHS model are listed in table 1 for the sensor configuration shown in figure 1.

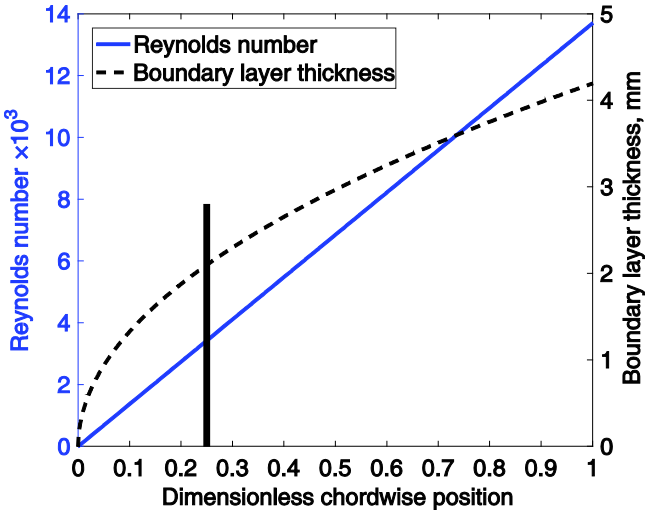

Figure 4. Reynolds number and boundary layer thickness along the chord of the baseline wing model, estimated using the nominal free stream speed.

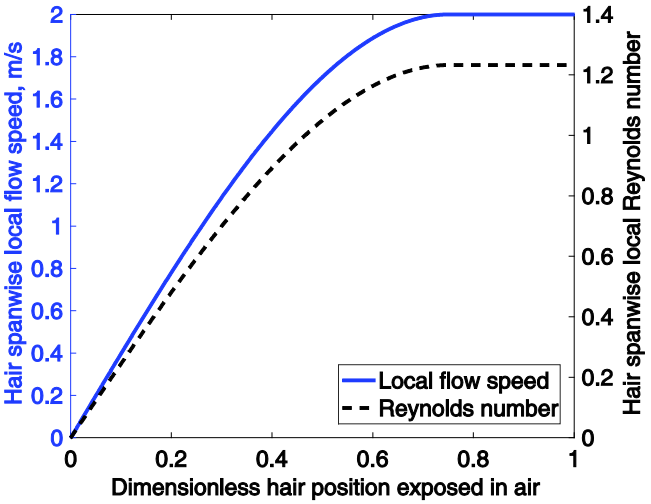

Figure 5. Local flow speed and Reynolds number along the hair exposed in air with nominal flow $U_\infty = 2.0\ \mathrm{m\,s^{-1}}$.

Table 1. Properties of a baseline artificial hair sensor.

Property	Value
Depth of hair inside capillary (l_1), mm	1.00
Hair length exposed in air (l_2), mm	2.80
Capillary inner diameter (D), μm	25.0
Hair diameter (d), μm	9.00
Hair/glass fiber Young's modulus (E), GPa	75
Compressive modulus of CNTs (κ), kPa	4.41
Equivalent spring constant (k), $\mathrm{N\,m^{-2}}$	3.90×10^3

The flow properties along the hair exposed in the air are then calculated and shown in figures 5 and 6. It can be seen that the Reynolds number with respect to the hair is extremely small, which verifies the laminar flow assumption. Due to the low Reynolds number, particularly in the region close to the surface, the drag coefficient on the hair may be very high.

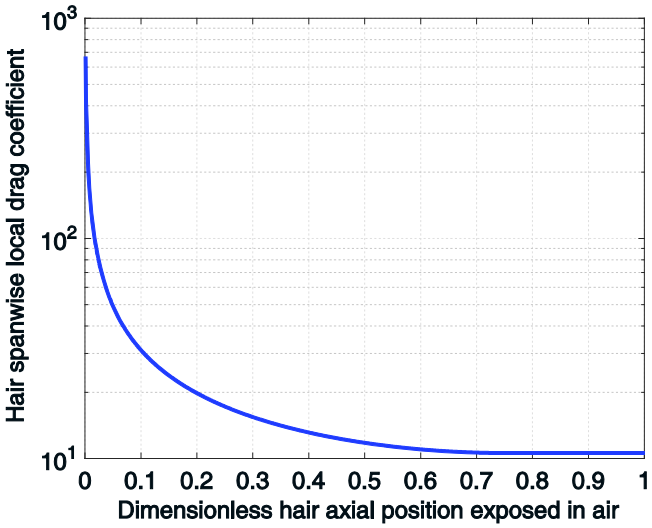

Figure 6. Local drag coefficient along the hair exposed in air with nominal flow $U_\infty = 2.0\ \mathrm{m\,s^{-1}}$.

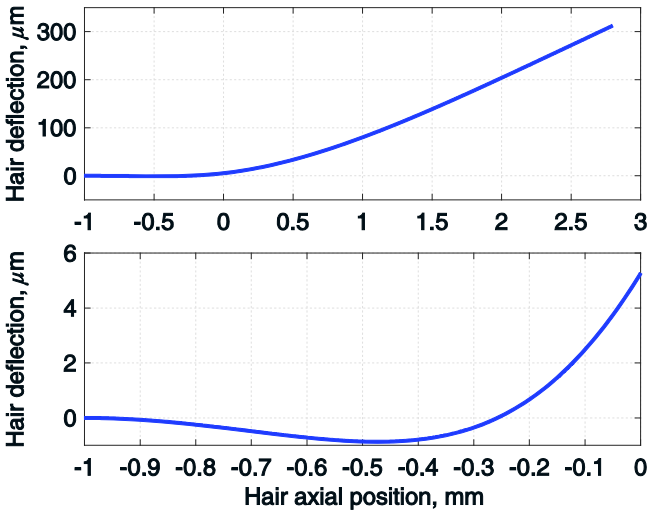

Figure 7. Deflection of baseline hair sensor with nominal flow $U_\infty = 2.0\ \mathrm{m\,s^{-1}}$.

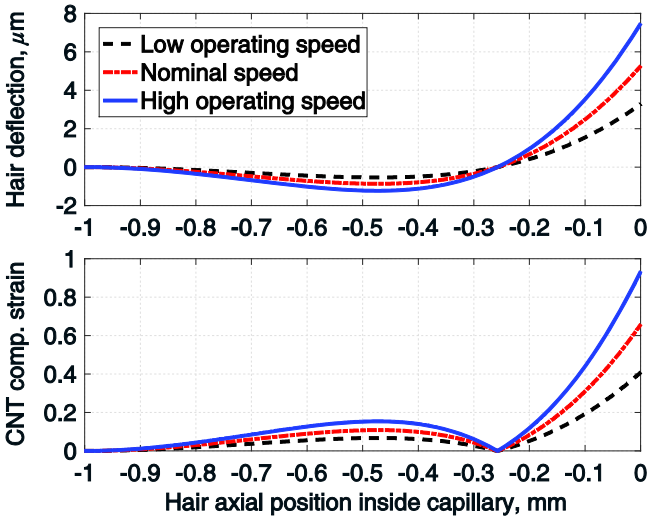

Figure 8. Deflection of baseline hair with flow speed of operating range.

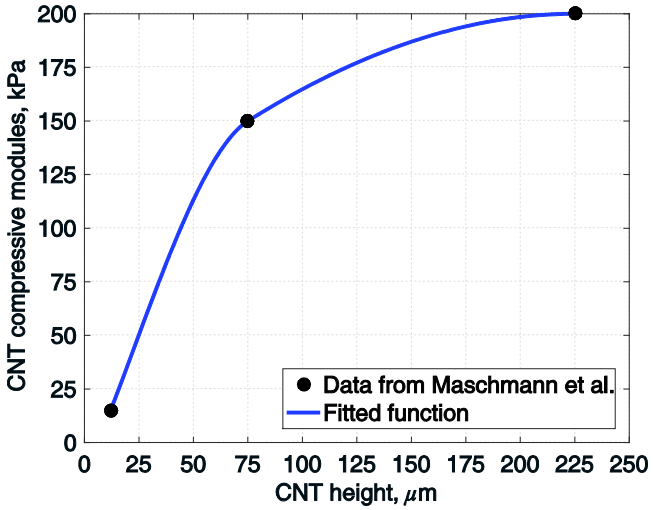

Figure 9. CNT compressive modules versus CNT height.

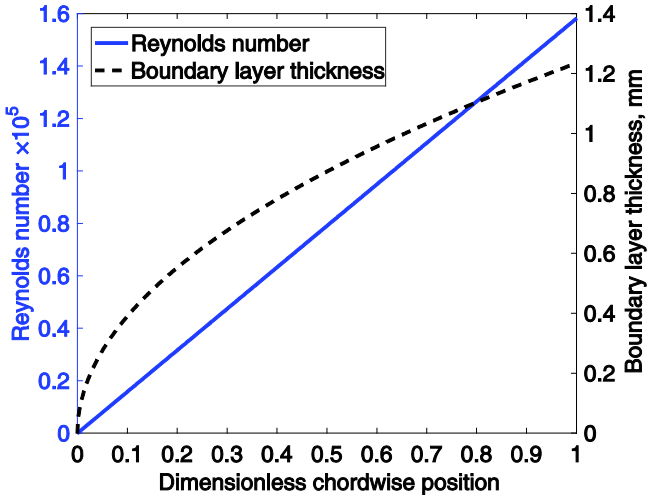

Figure 10. Reynolds number and boundary layer thickness of nominal Class 1 wing.

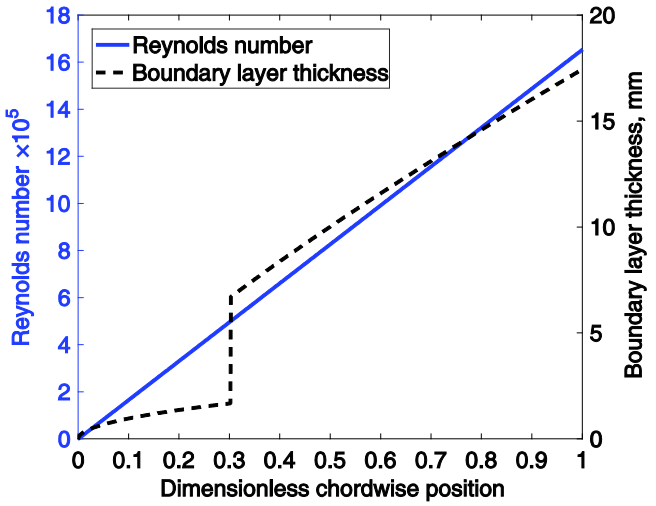

Figure 11. Reynolds number and boundary layer thickness of nominal Class 2 wing.

However, the resultant aerodynamic drag is still small, because of the very low local speed in the region. Finally, the deflection of the hair inside the capillary is calculated and plotted in figure 7. It is of interest to note the curvature change in the middle segment of the hair inside the capillary. It is also not surprising to see the largest deflection of the segment inside the capillary is at $x = 0$.

As discussed in a previous section, the nominal speed U_∞ is used to determine the boundary layer thickness around the airfoil. The shear flow speed distribution within the boundary layer is then determined by the local flow speed to be measured. In this case, we only consider the low and high limits of the sensors' operating range. They may cause quite different hair deflections and CNT compressive strains from the nominal flow speed (figure 8). Note the CNT strains at $x = 0$ are the values to be held constant when the hair sensor geometry is scaled. The minimum and maximum CNT compressive stains at $x = 0$ are 0.41 and 0.93, respectively, which are used to determine the operating range of the scaled AHSs.

3.2. Compressive modulus of CNTs

It has been reported that the compressive modules of CNTs are dependent on their height [15], with only limited discrete data provided in Maschmann *et al* [15]. Here, these data are used to fit a function using the piecewise cubic Hermite interpolation. This function is plotted in figure 9, which will be further used to provide a lookup table of the compressive modules of CNTs given any CNT height within the range.

3.3. Scaling of AHS for different aircraft

Three different types of aircraft with distinct dimensions, flight altitudes, and nominal speeds (table 2) are selected for this study. These aircraft types are selected to be representative of vehicles at different scales, and do not match any particular vehicle. Figures 10–12 show the chordwise Reynolds number and boundary layer thickness of the three classes of vehicles calculated using the nominal speeds. The Class 1 vehicle has a pure laminar boundary layer, while the other two see the transition from laminar to turbulent flows in the boundary layers. However, the transition points are behind the quarter chord. So the scaling of the sensor installed at the quarter chord can adopt the laminar flow condition in the boundary layer. Note that the boundary layer transition region is not modeled, so that figures 11 and 12 depict a discontinuity in thickness at the transition point. The actual boundary layer thickness is continuous; however, since the scaling exercise described here is only concerned with a single sensor position at the quarter-chord, this discrepancy will have no impact on the results of the study.

Following the procedure highlighted in figure 3, one can scale the dimensions of the AHSs suitable for the nominal flow conditions for these different aircraft. The dimensions of scaled sensors are listed in table 3. Figure 13 compares the length of the hairs scaled for the three classes of aircraft. As the hair length is mainly determined by the local boundary layer thickness, the resulting hair length for the Class 1

Table 2. Flight conditions of different classes of aircraft.

Property	Baseline	Class 1	Class 2	Class 3
Nominal speed (U_∞), m s^{-1}	2	25	60	170
Altitude (H), m	0	1000	8000	18 000
Air density (ρ), kg m^{-3}	1.225	1.112	0.526	0.120
Kinematic viscosity (ν), m^2 s^{-1}	1.46×10^{-5}	1.58×10^{-5}	2.90×10^{-5}	1.18×10^{-4}
Mean airfoil chord (c), m	0.10	0.10	0.80	1.20
Nominal Mach number	0.0059	0.074	0.19	0.58

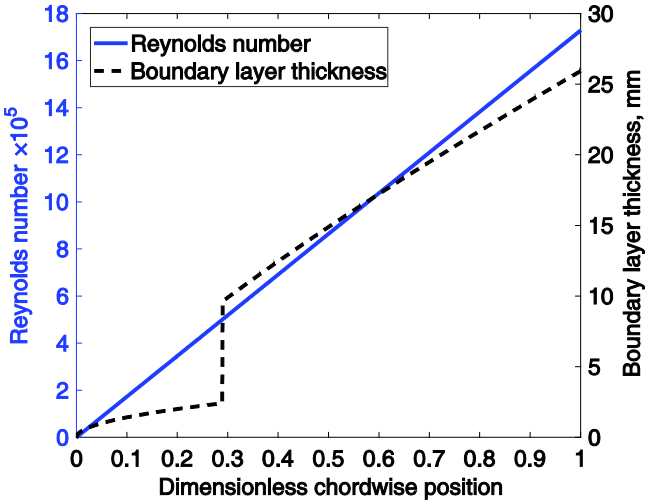

Figure 12. Reynolds number and boundary layer thickness of nominal Class 3 wing.

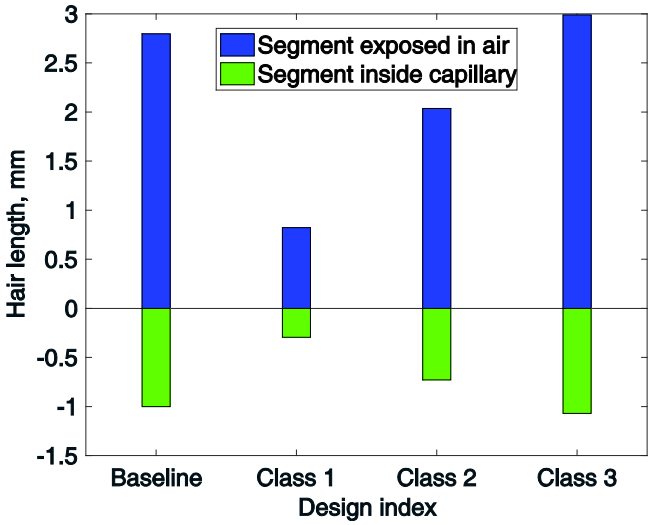

Figure 13. Scaled hair length inside the capillary and exposed in air for different classes of aircraft.

vehicle is much shorter than that of the baseline. This agrees with the very thin boundary layer of the Class 1 vehicle (figure 10). It is expected that the required hair length should be longer if the sensor is to be placed closer to the trailing edge. For the Class 3 vehicle, the boundary layer thickness at a quarter chord happens to be similar to the baseline, resulting in a very similar hair length as that of the baseline. It is also noticed that for the Classes 2 and 3 vehicles, the boundary layers transition from the laminar flow to the turbulent flow behind the quarter chord location, after which the boundary layers are much thicker (figures 11 and 12). Therefore, the required hair length, if used in this region, should be significantly longer than the current calculation at the quarter chord location. However, the current study does not calculate the scaling of the AHSs to be used in this region, due to the very complex flow condition in the turbulent boundary layer with potential separation of the boundary layer. Figure 14 plots the diameter parameters of the scaled AHSs. From the figure, it can be seen that the diameters are mainly impacted the by the magnitude of the flow speed. Table 3 also summarizes the local Reynolds numbers based on the local speed and the hair diameter.

3.4. Sensitivity and operating range of AHS

The previous scaling study uses only the nominal speed of each aircraft. However, the local flow speed along their airfoils varies in a very large range. For instance, the local flow speed along the top surface of the airfoil is greater than the nominal and it can be orders higher close to the leading edge. On the other hand, the local flow speed along the bottom surface of the airfoil is less than the nominal. Therefore, it is important to understand how the scaled AHS may work in such a wide speed range. Figure 15 shows the CNT compressive strain of the scaled AHS for the Class 2 vehicle across a range of flow speeds. Note that at the nominal speed of 120 m s^{-1}, the compressive strain is about 0.66, the same as the baseline sensor in its nominal flow condition (figure 8). This is simply because the scaling rule of the study keeps the CNT strain constant. From figure 8, the minimum and maximum CNT stains have been found and are used to determine the operating range of the scaled sensor, as marked out by the square and circle signs in figure 15. It is clear to see the operating range or bandwidth of this scaled AHS is about 42–78 m s^{-1}. Obviously, a single design of AHS is not able to work in the full range of local speeds along an airfoil. To find the AHSs that may work for different speeds, the scaling design of AHS for the Class 2 aircraft is further studied, where different operating speeds are used for the scaling from the baseline sensor. For simplicity, the length parameters of the scaled sensors are still the same as the previous, while the different operating speeds result in different diameters of the sensors (table 4). These sensors with identical length but different diameters are also evaluated with the varying flow speed and the resulting CNT compressive strains are plotted in figure 16. In the

Table 3. Scaled dimensions of AHS for different classes of aircraft.

		Class 1		Class 2		Class 3	
	Baseline	Value	Ratio	Value	Ratio	Value	Ratio
l_1, mm	1.00	0.294	0.294	0.728	0.728	1.068	1.068
l_2, mm	2.80	0.823	0.294	2.036	0.728	2.988	1.068
D, μm	25.0	29.620	1.185	65.193	2.608	105.520	4.221
d, μm	9.00	10.663	1.185	23.469	2.608	37.987	4.221
Nominal Re with d	1.233	16.862	—	48.488	—	54.697	—

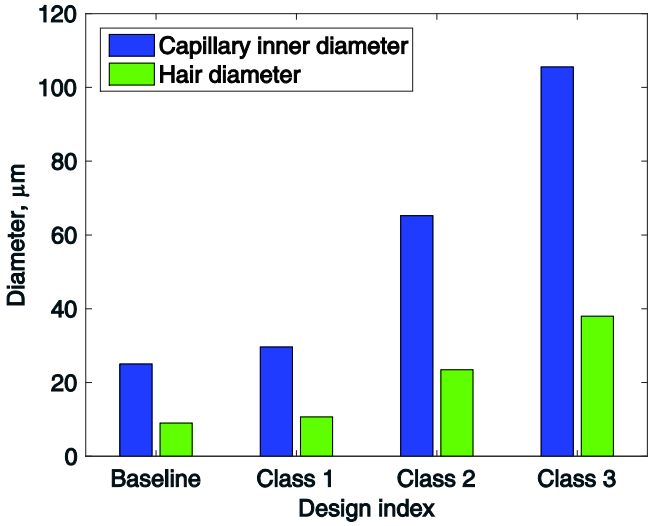

Figure 14. Capillary inner diameters and hair diameters of the AHSs for different classes of aircraft.

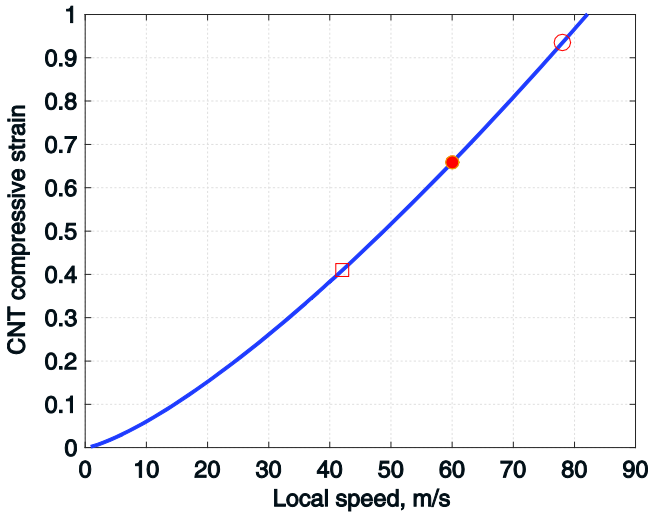

Figure 15. Operating range of the AHS scaled from nominal speed of Class 2 aircraft.

figure, the two horizontal dotted lines represent the cut-off limits of the CNT compressive strain, which clearly identify the operating bandwidths of each sensor with different operating speeds. From the plot, it can be seen that the thicker sensors have wider operating bandwidths and are suitable for measuring higher flow speeds. However, the thinner sensors are very

Table 4. Diameters of AHS for Class 2 vehicle with different operating speeds.

AHS	Speed, m s^{-1}	D, μm	d, μm
Baseline	2	9.000	7.609
Scaled	12	34.795	12.526
	20	42.037	15.133
	36	53.001	19.080
	65	67.333	24.240
	120	85.738	30.866

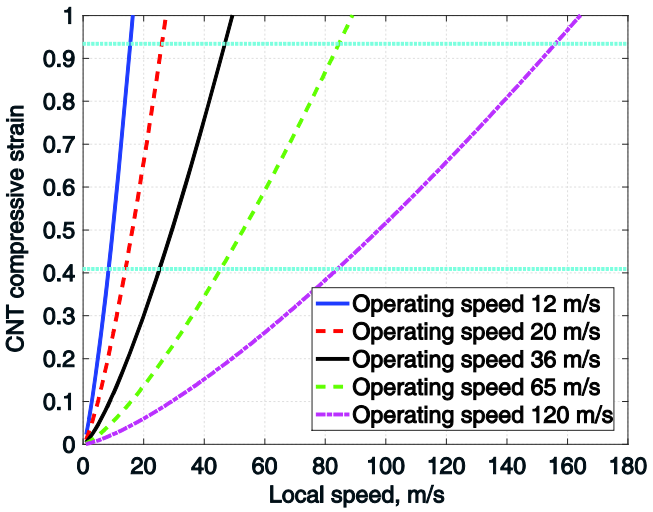

Figure 16. Bandwidth of AHSs with different operating speeds.

sensitive to the flow speed change and have very narrow operating bandwidths, resulting in difficulties in measuring the lower speeds. To resolve the issue, one may consider changing the materials of the hair and CNTs, so as to reduce the slope of the curves in figure 16 at lower speeds. Alternatively, it may be more efficient to use different piezoresistive materials that may respond to the compression from CNTs at a lower cut-off limit.

4. Conclusion

This paper presented an approach to properly size AHSs applicable to different flight vehicles and conditions. In doing so, the artificial hair was modeled as a linear Euler–Bernoulli beam with an elastic foundation and subject to the local shear

flow pressure. The aerodynamic drag on the hair was predicted based on the assumption of laminar flow in the boundary layer. The hair is deflected by the drag and presses the electrode mounted on the wall of the capillary. The electric current is dependent on the flow pressure and thus the compressive strain of CNTs grown along the artificial hair. Numerical studies were performed to design the AHSs for three different classes of aircraft scaled from the same baseline sensor. The sensor sizing parameters were separated into two groups. The length parameters of the hair were sized based on the local boundary layer thickness. The diameters of the hair and capillary were determined by keeping the same maximum compressive strain of the CNTs in the sensors. This rule may ensure the scaled sensor is still sensitive to the flow conditions of the different vehicles. The scaling approach has considered the electrical, material, structural and aerodynamic properties of the hairs/CNTs. To allow for measurements in a wide range of speeds, the AHS can be scaled for different operating speeds based on the same baseline sensor. However, the resulting sensors may have a very narrow operating bandwidth because of the thin diameter of the hair.

Even though this study presented a feasible approach to quickly design the hair sensors for the flow measurement of different vehicles, it was limited due to the assumption of the laminar boundary layer around the airfoil. A simple estimation of the boundary layer thickness based on a flat plate was used. Therefore, only the hairs to be installed within the first quarter chord region from the leading edge (of Class 2 and 3 vehicles) can be scaled using this approach. For the Class 3 vehicle, there may also be other impacts due to transonic flow locally on the top surface of the airfoil, depending on operating conditions, which would require additional modification to the aerodynamic model in the study. Finally, CFD simulations are suggested to make sure the scaled sensors will not significantly impact the original flow around the wing/airfoil.

Acknowledgments

This work was supported by the US Air Force Summer Faculty Fellowship. This paper has been cleared for public release, case number 88ABW-2017-0202.

References

[1] Mangalam A S and Brenner M J 2014 Fly-by-feel sensing and control: aeroservoelasticity *AIAA Atmospheric Flight Mechanics Conf. (Atlanta, GA, 16–20 June)* AIAA-2014-2189

[2] Shen H, Xu Y and Dickinson B T 2014 Fault tolerant attitude control for small unmanned aircraft systems equipped with an airflow sensor array *Bioinsp. Biomim.* **9** 046015

[3] Guerreiro N and Hubbard J 2008 Pressure port placement for lift distribution measurement on a model aircraft with optimized trailing-edge flaps *26th AIAA Applied Aerodynamics Conf. (Honolulu, HI, 18–21 August)* AIAA-2008-7518

[4] Bekey G A 2005 *Autonomous Robots: From Biological Inspiration to Implementation and Control* (Cambridge, MA: MIT Press)

[5] Sterbing-D'Angelo S, Chadha M, Chiu C, Falk B, Xian W, Barcelo J, Zook J M and Moss C F 2011 Bat wing sensors support flight control *Proc. Natl Acad. Sci. USA* **108** 11291–6

[6] Dickinson B, McClain S and Case L 2012 The dynamic response of quasi-steady hair-like structures in oscillatory boundary layer flows *6th AIAA Flow Control Conf. (New Orleans, LA)* AIAA-2012-3048

[7] McClain S, Case L and Dickinson B 2012 Response of passive surface hairs in steady falkner-skan boundary layers *6th AIAA Flow Control Conf. (New Orleans, LA)*

[8] Dickinson B, Singler J and Batten B 2006 Modeling of bioinspired sensors for flow separation detection in micro air vehicles *3rd AIAA Flow Control Conf. (San Francisco, CA)* AIAA-2006-3019

[9] McClain S, Case L and Brown C 2013 A flap-based gust generation system for hair sensor investigations *51st AIAA Aerospace Sciences Meeting including the New Horizons Forum and Aerospace Exposition (Grapevine, TX)* AIAA-2013-1131

[10] Dickinson B, Singler J and Batten B 2008 The detection of unsteady flow separation with bioinspired hair cell sensors *26th AIAA Aerodynamic Measurement Technology and Ground Testing Conf. (Seattle, WA)* AIAA-2008-3937

[11] Phillips D M, Ray C W, Hagen B J, Su W, Baur J W and Reich G W 2015 Detection of flow separation and stagnation points using artificial hair sensors *Smart Mater. Struct.* **24** 115026

[12] Su W and Reich G W 2016 Artificial hair sensor designs for flow measurement of UAVs with different scales *SPIE Smart Structures/NDE Conf. 2016 (Las Vegas, NV, 20–24 March)* 98031W

[13] Slinker K, Kondash C, Maschmann M, Severin B, Reich G W, Dickinson B T and Baur J 2015 Artificial hair sensors from structural microfibers and CNT arrays for sensing air flow or mechanical shear *20th Int. Conf. on Composite Materials (Copenhagen, Denmark, 19–24 July)*

[14] Phillips D M, Slinker K A, Ray C W, Hagen B J, Baur J W, Dickinson B T and Reich G W 2014 Artificial hair sensors: electro-mechanical characterization *ASME 2014 Conf. on Smart Materials, Adaptive Structures and Intelligent Systems (Newport, RI, 8–10 September)*

[15] Maschmann M R, Dickinson B, Ehlert G J and Baur J W 2012 Force sensitive carbon nanotube arrays for biologically inspired airflow sensing *Smart Mater. Struct.* **21** 094024